RAPID COMMUNICATIONS

PHYSICAL REVIEW MATERIALS **1**, 031401(R) (2017)

Robust spin current generated by the spin Seebeck effect

Feng-Jen Chang,[1] Jauyn Grace Lin,[2] and Ssu-Yen Huang[1,*]
[1]*Department of Physics, National Taiwan University, Taipei 10617, Taiwan*
[2]*Center for Condensed Matter Sciences, National Taiwan University, Taipei 10617, Taiwan*

(Received 17 March 2017; published 30 August 2017)

Spin pumping (SP) and the spin Seebeck effect (SSE), two of the most common methods for generating a pure spin current from ferromagnetic insulators, are considered to share similar physical mechanisms. However, a systematic study of the fundamental difference of their working principle is missing. In this Rapid Communication, we present experimental evidence of the contrast in a pure spin current generated by SP and SSE, based on results from yttrium iron garnet (YIG) with various crystalline properties. It is shown that while the SP-induced spin current could be two-orders-of-magnitude different between the polycrystalline and epitaxial films, the SSE-excited spin current is surprisingly insensitive to the different crystal structures. Our results clearly distinguish the coherent mechanism of SP from the noncoherent mechanism of the SSE. Consequently, the robust SSE voltage against poor crystallinity proves that the SSE is a powerful tool to explore pure spin current physics, and suggests that polycrystalline YIG films are a promising candidate for spin caloritronic applications.

DOI: 10.1103/PhysRevMaterials.1.031401

The growing development of spintronics and spin caloritronics has recently demonstrated the great advantage of exploiting pure spin current phenomena. Among the progress shown, a pure spin current generated by a ferromagnetic insulator (FMI) such as yttrium iron garnet ($Y_3Fe_5O_{12}$, YIG) [1–4] provides unequivocal experimental results, since it eliminates the accompanying charge current and the signal shunting effect from the conductive layer. It is also a preferable technology for developing future memory devices with less power consumption.

To generate a pure spin current from an FMI, spin pumping (SP) and the spin Seebeck effect (SSE) are currently the most applicable and established methods. Figure 1 illustrates the spin-to-charge current conversion by the two methods in a commonly used normal metal (NM)/FMI heterostructure. In both cases, the pure spin current can be detected as a transverse electric (TE) field in an NM layer with a strong spin-orbit coupling, such as 5*d* metals (Pt, W, Au, Ta, etc.) [5,6] and 3*d* metals (Py, Co, Cr, etc.) [7–10], due to the inverse spin Hall effect (ISHE). When the FMI is in a ferromagnetic resonance (FMR) state, the coherent precession motion of the magnetic moments in the FMI injects a pure spin current into the adjacent NM layer by the SP, as shown in Fig. 1(a). On the other hand, a longitudinal temperature gradient in the FMI can also generate a pure spin current, as demonstrated in Fig. 1(b), which is termed the longitudinal SSE (LSSE) configuration. Consequently, the magnitude of the SSE signal is proportional to the temperature gradient, and that of the SP signal is proportional to the microwave power.

The SSE is often described as a *thermal spin pumping* effect since it shares a similar mechanism with SP, only that the precession motions of the magnetic moments in the SSE are noncoherently excited by thermal energy [11–14]. In principle, the highly coherent precession motion driven by FMR requires a monocrystalline FMI layer with high homogeneity, while noncoherent thermal motions are insensitive to crystallinity. Although the SSE and the SP have been widely studied, this crucial point, the difference between coherent and noncoherent mechanisms, has yet to be addressed. Our results not only show that the effect of different crystallinity on the propagation of spin-wave spin current plays different roles, but also highlight the distinct mechanism in $k = 0$ and $k \neq 0$ magnon modes. Moreover, we explore several applications in spintronics based on our findings.

In this Rapid Communication, both epitaxial and polycrystalline YIG thin films are simultaneously fabricated by using different substrates under the same fabrication conditions. We systematically study and compare the SP and the SSE in YIG with different crystallinities. The precession motion of spin waves excited from the SP and SSE can either be localized or propagated through the magnetic materials. Our results reveal that the SP-ISHE voltage is significantly suppressed in polycrystalline YIG, while the SSE-ISHE voltage is robust against poor YIG crystallinities. Such different responses to the crystal structure not only reflect the different excitation energies and mechanisms of the two phenomena, but also open up potential applications of polycrystalline YIG in spintronic devices.

A typical rf magnetron sputtering system is used to deposit YIG thin films with a thickness of 58 nm on single crystals of gadolinium gallium garnet (GGG) (111) and Si (100), and glass substrates at room temperature. The as-deposited YIG films are amorphous and nonmagnetic, and are subsequently crystallized by *ex situ* postannealing at various temperatures from 600 to 1000 °C, in an oxygen atmosphere with ambient pressure. The sample dimensions for the SP measurement are 1 mm × 3 mm, while those for the SSE measurement are 3 mm × 5 mm. A 6-nm-thick Pt layer is deposited on the top of the YIG samples above by magnetron sputtering to detect the pure spin current. The magnetic hysteresis loops of YIG slabs and films are measured with a vibrating sample magnetometer (VSM). The SP experiment is conducted by sweeping the external magnetic field with a microwave frequency of 9.77 GHz in a TE_{102} cavity at room temperature [15]. To generate a pure spin current by the SSE, we employ a longitudinal experimental setup with a heater and a heat

---

[*] syhuang@phys.ntu.edu.tw

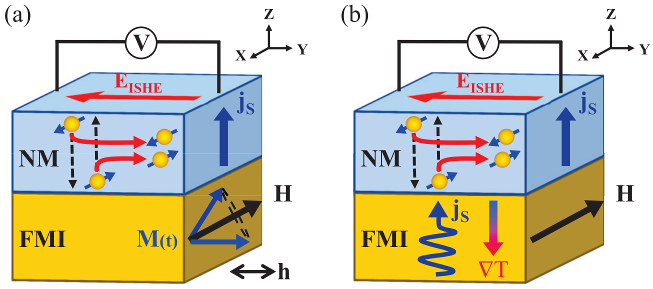

FIG. 1. Schematic illustration of spin current generation from (a) SP and (b) SSE in an NM/FMI structure.

sink [16–18] to generate a uniform out-of-plane temperature gradient with 4.8-W heating power.

For comparison, we also conduct the experiments on single-crystal and polycrystalline YIG slabs with thicknesses of 0.9 and 0.5 mm, respectively. The crystal structures and orientations of YIG are determined by x-ray diffraction (XRD) and transmission electron microscopy (TEM), as shown in Fig. 2. The XRD pattern of the single-crystal YIG slab only shows the (222) and the (444) peaks in Fig. 2(a), while that of the polycrystalline slab displays multiple peaks corresponding to different crystal orientations in Fig. 2(d). The full width at half maximum (FWHM) of the (444) peak in Fig. 2(a) and that of the (420) peak in Fig. 2(d) are both around 0.065°. For the thin films, owing to a good lattice match between YIG (12.376 Å) [19] and GGG (12.382 Å) [20], the XRD pattern of the YIG/GGG shows a series of peaks corresponding to the (111) orientation in Fig. 2(b). The main peak is the (444) peak, with an FWHM of 0.055°, implying high-quality epitaxial growth. However, the YIG films grown on the Si substrate with a lattice constant of 5.431 Å [21] and on the amorphous glass substrate have polycrystalline structures with multiple XRD peaks, (400), (420), and (422), and wide FWHM (around 0.16°), as shown in Fig. 2(e). TEM also confirms the well-oriented lattices with a sharp interface between the epitaxial YIG film and the GGG substrate in Fig. 2(c), while the polycrystalline structure of YIG on Si or glass is shown in Fig. 2(f).

Magnetic hysteresis loops of both the YIG slabs and the films are plotted in Fig. 3. The single-crystal and polycrystalline YIG slabs show similar magnetic properties with a saturated magnetization (M_S) around 140 emu/cm^3 and a coercive field (H_C) of less than 1 Oe in Fig. 3(a). On the other hand, the H_C of the polycrystalline YIG films on Si and glass (~20 Oe) are 40× larger than that of the epitaxial film on GGG (~0.5 Oe) in Fig. 3(b), although they have similar values of M_S. According to the grain-boundary-limited-wall model [22], the large H_C of the polycrystal YIG films may be due to the small grain size, which is estimated to be around 0.14 μm.

To understand the effect of crystallinity on the magnetic properties of the samples, we systematically change the annealing temperature for both the epitaxial and polycrystalline films. In Fig. 3(c), the polycrystalline films show a significantly larger H_C than that of the epitaxial films, regardless of the annealing temperature. The M_S of the films are found to first increase and then decrease with increasing annealing temperature in Fig. 3(d). The enhancement of M_S in the low-temperature range is due to the crystallization process of YIG thin films. The crystallization temperature for YIG/Si and YIG/glass is around 750 °C, while it is 650 °C for YIG/GGG, consistent with the values reported in the literature [23–26]. The slight decrease of M_S at temperatures above 850 °C may be caused by the formation of non-YIG phases or/and interfacial diffusion. The annealing experiment confirms 750 °C to be an optimal annealing temperature for all samples. Hence, the following analysis on the SP and the LSSE results is mainly for the 750 °C annealed samples.

Figure 4(a) shows normalized FMR spectra as functions of the in-plane magnetic field around the resonance field (H_R) for three YIG films. It is clear that the intensity and the linewidth of the YIG/GGG film are respectively much larger and much narrower than those of the YIG/Si and YIG/glass

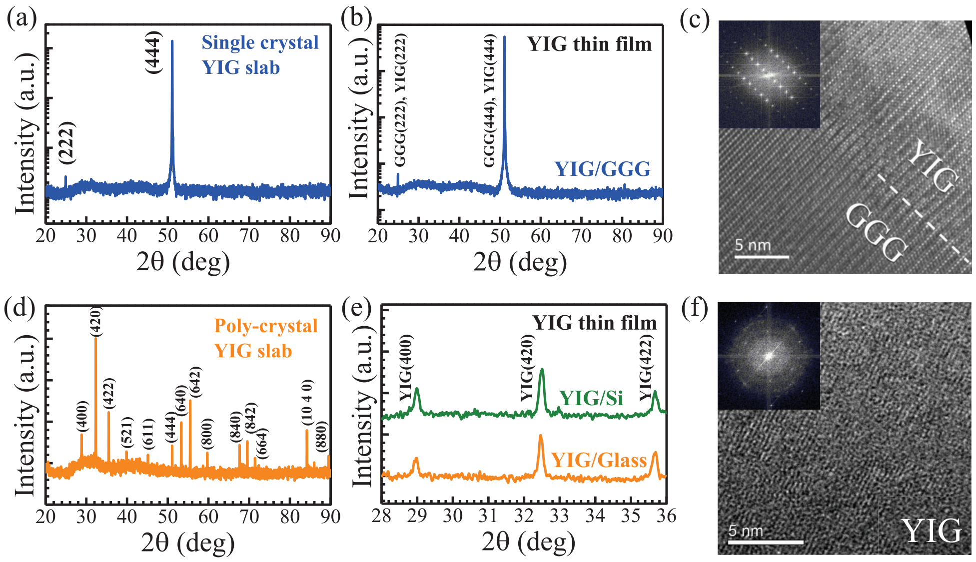

FIG. 2. XRD patterns for (a) single-crystal and (d) polycrystalline YIG slabs, and YIG thin films grown on (b) GGG, (e) Si, and glass. Cross-section TEM images and their fast Fourier transformation (insets) for YIG thin films grown on (c) GGG and (f) Si.

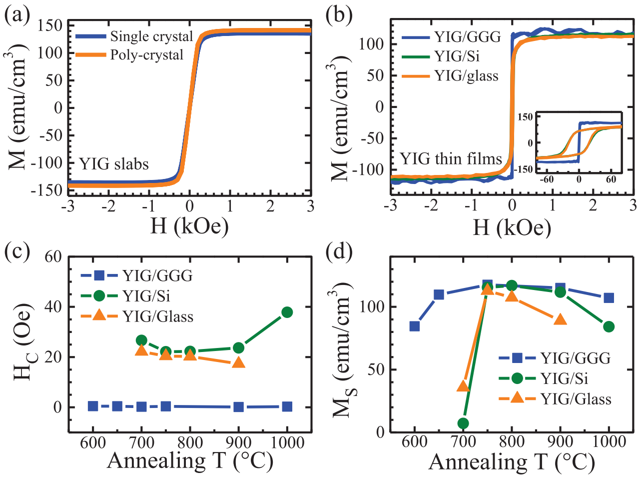

FIG. 3. Magnetic hysteresis loops of (a) single-crystal and polycrystalline YIG slabs, and (b) YIG thin films. The inset of (b) is in a small field range. Annealing-temperature dependence of (c) H_C and (d) M_S of YIG thin films.

films. By fitting the FMR derivative spectrum of YIG/GGG with a differential Lorentzian curve (solid line) as shown in Fig. 4(b), the peak-to-peak linewidth (H_{PP}) is estimated at (5.0 ± 0.4) Oe, reflecting a high crystalline quality [27–29]. The maximum intrinsic damping constant α_{YIG} is extracted at $(1.2 \pm 0.1) \times 10^{-3}$ from the general formula $H_{\mathrm{PP}} = \frac{2}{\sqrt{3}}\alpha(\frac{\omega}{\gamma})$ [30], where ω is the angular frequency of the microwave, and γ is the gyromagnetic ratio of YIG. In contrast, the values of α_{YIG} for the YIG/Si and the YIG/glass polycrystalline films are respectively $(3.0 \pm 0.7) \times 10^{-2}$ and $(2.2 \pm 0.4) \times 10^{-2}$. These values are up to 20× larger than that of the epitaxial YIG/GGG film. The complex and broad resonance spectra of the polycrystalline films should be caused by the overlapping of the resonance spectra from different crystal grains, in which the randomly oriented magnetic anisotropy axes result in stronger damping and poorer FMR absorption intensities due to the two-magnon scattering mechanism [31–34].

Figure 4(c) plots the SP-ISHE voltage normalized by the microwave powers and distances between the electric contacts on Pt. The voltage from the epitaxial YIG film is much larger (two orders of magnitude) than that from the polycrystalline films, agreeing with their FMR spectra in Fig. 4(a). It is worth mentioning that the value of the SP-ISHE voltage in the Pt/YIG/GGG sample is 1.8 μV/mm, comparable to that in the high-quality sputtered epitaxial YIG film reported by Wang *et al.* [27], if normalized by microwave power.

Based on the peak-to-peak linewidth, the effective damping constants $\alpha_{\mathrm{Pt/YIG}}$ for the Pt/YIG/GGG, Pt/YIG/Si, and Pt/YIG/glass are obtained as $(2.2 \pm 0.3) \times 10^{-3}$, $(3.3 \pm 0.3) \times 10^{-2}$, and $(2.3 \pm 0.2) \times 10^{-2}$, respectively, with a one-order-of-magnitude difference between the values of the epitaxial and the polycrystalline YIG. Furthermore, the model of the SP provides the formula for spin current density as

$$J_S^0 = \frac{g_r^{\uparrow\downarrow} h^2 \hbar \gamma^2}{8\pi(\alpha_{\mathrm{Pt/YIG}})^2}\left[\frac{4\pi M_e \gamma + \sqrt{(4\pi M_e)^2\gamma^2 + 4\omega^2}}{(4\pi M_e)^2\gamma^2 + 4\omega^2}\right], \tag{1}$$

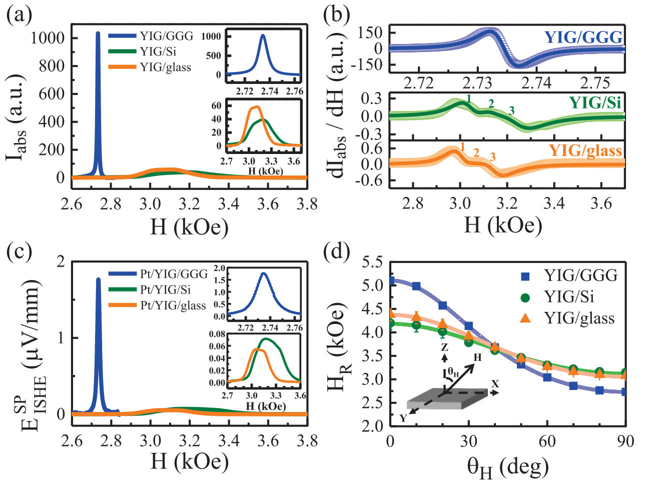

FIG. 4. Results of FMR and SP measurements on YIG thin films. (a) Normalized FMR absorption intensity. (b) Derivatives of the FMR spectra. The solid lines are the fitting lines. (c) ISHE signal by SP. The insets of (a) and (c) are zoom-in results. Signals in (a)–(c) are normalized to 1-mW microwave power. (d) Measured H_R as a function of θ_H, which is defined in the inset. The solid lines are the fitting lines.

where h^2 is the square of the microwave magnetic field, $\hbar$ the reduced Planck constant, γ the gyromagnetic ratio, and $4\pi M_e$ the effective demagnetization field of YIG [35]. By measuring the H_R as a function of θ_H in Fig. 4(d), γ is experimentally derived as $(1.77 \pm 0.05) \times 10^{11}\ \mathrm{s}^{-1}\ \mathrm{T}^{-1}$ for the three samples, and $4\pi M_e$ for YIG/GGG, YIG/Si, and YIG/glass are 1647 ± 1, 721 ± 173, and 898 ± 138 Oe, respectively [30]. The relatively smaller $4\pi M_e$ for the polycrystalline films is due to the perpendicular magnetic anisotropy induced by the magnetoelastic effect during annealing [36,37]. Another important parameter in Eq. (1) is the real part of the spin mixing conductance ($g_r^{\uparrow\downarrow}$), which reflects the spin-injection efficiency. The $g_r^{\uparrow\downarrow}$ is experimentally estimated at $(4.3 \pm 1.4) \times 10^{18}$, $(1.3 \pm 3.0) \times 10^{18}$, and $(4.2 \pm 10.8) \times 10^{18}\ \mathrm{m}^{-2}$ for Pt/YIG on GGG, Si, and glass, respectively, based on

$$g_r^{\uparrow\downarrow} = \frac{4\pi M_S d_{\mathrm{YIG}}}{g\mu_B}(\alpha_{\mathrm{Pt/YIG}} - \alpha_{\mathrm{YIG}}), \tag{2}$$

where d_{YIG} is the thickness of the YIG layer, μ_B the Bohr magneton, and $g = \hbar\gamma/\mu_B$ the g-factor of YIG [35]. Interestingly, the value of $g_r^{\uparrow\downarrow}$ is roughly the same for the epitaxial and polycrystalline YIG films. Therefore, the most important parameter to cause the very distinct SP-ISHE voltage for epitaxial and polycrystalline YIG must be $\alpha_{\mathrm{Pt/YIG}}$. Since the spin current is inversely proportional to the square of $\alpha_{\mathrm{Pt/YIG}}$ in Eq. (1), it is expected that the one-order-of-magnitude larger damping constants of the polycrystalline films produce two-orders-of-magnitude smaller ISHE signals than those of the epitaxial film.

The LSSE-ISHE voltage is detected in Pt along the long side of the samples, while the direction of magnetization, hence the spin index of the spin current, is aligned in the short side by an in-plane external magnetic field. Figure 5(a) demonstrates the field dependence of the LSSE-ISHE voltage in Pt/YIG

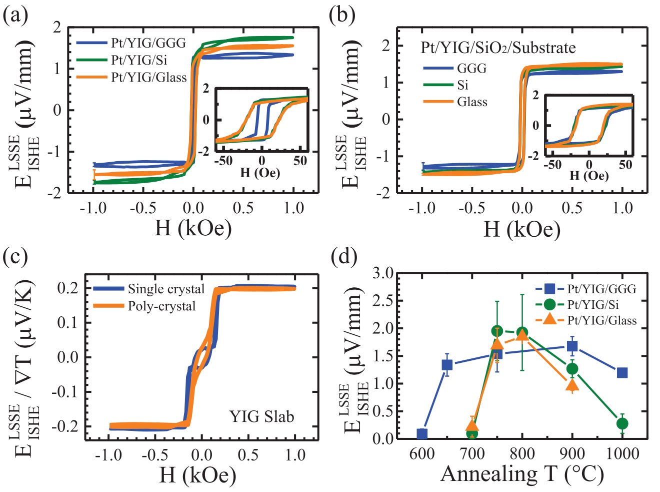

FIG. 5. Field dependence of the LSSE voltage measured in Pt on (a) YIG thin films, (b) YIG thin films with a SiO_2 insertion layer, and (c) YIG slabs. (d) Saturation LSSE-ISHE voltage as a function of annealing temperature for various YIG thin films.

thin films, normalized by the distances between the electrical contacts on Pt. First, we note that H_C for the epitaxial YIG film is much smaller than that for polycrystalline films, as shown in the inset, consistent with the magnetization hysteresis loop. Most interestingly and importantly, the saturation value of the LSSE-ISHE voltage is comparable among the three samples, contrary to the large difference between their SP signals. Because the LSSE-ISHE voltage is proportional to the longitudinal temperature gradient in YIG (∇T_{YIG}), the slight difference among the three signals may be due to the small variations of ∇T_{YIG} in the three samples. In the heat equation, $\nabla T \propto (q/\kappa)$, where q is the heat flux density in YIG and κ is the thermal conductivity of YIG, one expects that q is identical in the three YIG films, since a constant heating power is applied. Only small variations of κ in the epitaxial and polycrystalline films may cause the different values of ∇T_{YIG}.

To confirm the influence of crystallinity, we insert a thick SiO_2 layer (60 nm) between the YIG thin films and the substrates. Since the SiO_2 layer is amorphous and thick enough, the YIG thin films should all form polycrystalline structures after annealing, regardless of the substrates. As shown in Fig. 5(b), the similarly large H_C of the three LSSE-ISHE voltages confirm the polycrystalline nature of these YIG. Moreover, the very close saturation voltages demonstrate that ∇T_{YIG} is indeed identical in the three YIG thin films. This result not only verifies the constant q in this experimental setup, but also indicates that the LSSE can be a sensitive tool to indirectly probe the ∇T in a thin film.

To obtain the real value of an out-of-plane ∇T in YIG, we perform LSSE measurements by using single-crystal and polycrystalline YIG slabs with Pt on them under the same experimental conditions. ∇T_{YIG} is directly measured by inserting two thermal couples on the top and bottom of a sample. The LSSE-ISHE voltages are then normalized by the measured ∇T_{YIG}, which is around 13.4 K/mm in the single-crystal slab and 15.4 K/mm in the polycrystalline slab, as shown in Fig. 5(c). The results are similar to those for the thin films, where the saturation values are very close in the single-crystal and polycrystalline YIG slabs, confirming that the crystallinity of YIG is irrelevant to the SSE. Therefore, we conclude that the SSE can generate a robust pure spin current against the poor crystallinity of YIG.

The average grain (crystallite) size L from the XRD measurement can be evaluated by using the Scherrer equation $L = K\lambda/\beta\cos\theta$, where λ is the x-ray wavelength, β is the FWHM of the diffraction peak, and K is a constant related to the crystallite shape, which can be taken as 0.9 [38] here. However, this analysis is meaningful only for a size smaller than 100 nm due to instrumental broadening. According to the XRD measurement results, we obtain that the average grain sizes of the polycrystalline YIG thin films on Si and on glass are both around 52 nm, but that the average grain sizes of the YIG crystals and that of the epitaxial YIG thin film on GGG exceed the detection limit. Recent work suggests that the low-frequency magnons, whose energies are less than $\sim$30 K, resulting in a wavelength around 6.8 nm, provide a dominant contribution to the LSSE [39]. In contrast, the magnon propagation length could be of the order of several 100 nm to μm [40,41]. Therefore, our results suggest that a grain size that is smaller than the magnon propagation length but larger than the wavelength of the magnon is beneficial to generate a robust magnon spin current.

From our results, while the SP is sensitive to the crystal structure of YIG due to the influence of α, the SSE is not. This reveals the difference in the mechanisms of SP and the SSE. The coherent FMR that leads to SP requires a homogeneous FMI layer, thus it is largely suppressed in inhomogeneous polycrystalline films with a large α. However, although the detailed origin of the SSE is still under discussion, it is obvious that the spin current is generated by thermally excited noncoherent motions. Note that in the linear-response theory of the SSE, the spin current is mainly proportional to the temperature difference between the magnons and the electrons [11,42]. In the bulk-magnon-spin-current model, the spin current is generated by the magnon in the bulk of the FM. In both models, α is not a decisive factor [14,43]. Since the thermal energy can easily excite magnon modes of any wave number k and energy E, the SSE could stimulate spin currents initiated by magnons more efficiently than the SP [44,45].

Lastly, the annealing effect on the SSE is investigated. Figure 5(d) plots the annealing-temperature dependence of the saturated LSSE-ISHE voltage. The behavior is similar to that of the M_S in Fig. 3(d), where a rise in the voltage is followed by a decline with increasing annealing temperature, revealing a close relation between the SSE signal and the M_S of YIG. This result clearly shows that under the same saturation magnetization, the SSE can generate a robust spin current even in YIG with poor crystallinity. Therefore, it is evident that the SSE can be a better tool than the other methods to generate a pure spin current for exploring spin transport phenomena, especially the ISHE-related topic. It also implies that the polycrystalline YIG thin films fabricated on various types of substrates have a high potential and flexibility for applications of spin caloritronic devices.

In summary, we use Pt/YIG bilayer samples to investigate the difference in the mechanism of the SP and the SSE with a systematical comparison on the crystalline effect of the spin-to-charge current conversion. We found that while the SP generates a much smaller spin current in polycrystalline YIG films due to larger damping constants compared with the epitaxial film, the SSE-excited spin current is contrarily insensitive to the crystallinity of YIG. Most importantly, it reflects the difference between the FMR-driven coherent mechanism of the SP and the thermally excited noncoherent mechanism of the SSE. Our experimental results demonstrate that the SSE can generate a robust spin current, serving as a powerful tool to explore pure spin current physics. Furthermore, it is suggestive that polycrystalline YIG thin films are promising for spin caloritronic applications.

The authors would like to thank Professor J. H. Hsu and Dr. M. W. Chu of National Taiwan University for experimental support. This work was supported by the Ministry of Science and Technology of Taiwan under Grants No. MOST 103-2212-M-002-021-MY3 and No. MOST 105-2112-M-002-010-MY3. S.Y.H. acknowledges support via the Golden Jade Fellowship of the Kenda Foundation, Taiwan.

[1] G. E. W. Bauer, E. Saitoh, and B. J. Van Wees, Nat. Mater. **11**, 391 (2012).

[2] K. C. Uchida, H. Adachi, T. Kikkawa, A. Kirihara, M. Ishida, S. Yorozu, S. Maekawa, and E. Saitoh, Proc. IEEE **104**, 1946 (2016).

[3] A. Hoffmann, IEEE Trans. Magn. **49**, 5172 (2013).

[4] J. Sinova, S. O. Valenzuela, J. Wunderlich, C. H. Back, and T. Jungwirth, Rev. Mod. Phys. **87**, 1213 (2015).

[5] H. L. Wang, C. H. Du, Y. Pu, R. Adur, P. C. Hammel, and F. Y. Yang, Phys. Rev. Lett. **112**, 197201 (2014).

[6] D. Qu, S. Y. Huang, B. F. Miao, S. X. Huang, and C. L. Chien, Phys. Rev. B **89**, 140407 (2014).

[7] B. F. Miao, S. Y. Huang, D. Qu, and C. L. Chien, Phys. Rev. Lett. **111**, 066602 (2013).

[8] H. L. Wang, C. H. Du, P. C. Hammel, and F. Y. Yang, Appl. Phys. Lett. **104**, 202405 (2014).

[9] D. Qu, S. Y. Huang, and C. L. Chien, Phys. Rev. B **92**, 020418 (2015).

[10] D. Tian, Y. F. Li, D. Qu, S. Y. Huang, X. F. Jin, and C. L. Chien, Phys. Rev. B **94**, 020403 (2016).

[11] J. Xiao, G. E. W. Bauer, K. C. Uchida, E. Saitoh, and S. Maekawa, Phys. Rev. B **81**, 214418 (2010).

[12] K. Uchida, T. Ota, H. Adachi, J. Xiao, T. Nonaka, Y. Kajiwara, G. E. W. Bauer, S. Maekawa, and E. Saitoh, J. Appl. Phys. **111**, 103903 (2012).

[13] H. Adachi, K. C. Uchida, E. Saitoh, and S. Maekawa, Rep. Prog. Phys. **76**, 036501 (2013).

[14] S. M. Rezende, R. L. Rodríguez-Suárez, R. O. Cunha, A. R. Rodrigues, F. L. A. Machado, G. A. Fonseca Guerra, J. C. Lopez Ortiz, and A. Azevedo, Phys. Rev. B **89**, 014416 (2014).

[15] G. Y. Luo, J. G. Lin, W.-C. Chiang, and C.-R. Chang, Sci. Rep. **7**, 6612 (2017).

[16] K. C. Uchida, H. Adachi, T. Ota, H. Nakayama, S. Maekawa, and E. Saitoh, Appl. Phys. Lett. **97**, 172505 (2010).

[17] P. H. Wu and S. Y. Huang, Phys. Rev. B **94**, 024405 (2016).

[18] Y. J. Chen and S. Y. Huang, Phys. Rev. Lett. **117**, 247201 (2016).

[19] R. C. Linares, R. B. McGraw, and J. B. Schroeder, J. Appl. Phys. **36**, 2884 (1965).

[20] H. L. Glass and L. A. Moudy, J. Appl. Crystallogr. **7**, 22 (1974).

[21] W. O'Mara, R. B. Herring, and L. P. Hunt, *Handbook of Semiconductor Silicon Technology* (Crest Publishing House, New Delhi, 2007).

[22] A. Globus and M. Guyot, Phys. Status Solidi B **52**, 427 (1972).

[23] M. B. Park and N. H. Cho, J. Magn. Magn. Mater. **231**, 253 (2001).

[24] S. Yamamoto, H. Kuniki, H. Kurisu, M. Matsuura, and P. Jang, Phys. Status Solidi A **201**, 1810 (2004).

[25] N. Kumar, S. Prasad, D. S. Misra, N. Venkataramani, M. Bohra, and R. Krishnan, J. Magn. Magn. Mater. **320**, 2233 (2008).

[26] T. Goto, M. C. Onbaşlı, and C. A. Ross, Opt. Express **20**, 28507 (2012).

[27] H. L. Wang, C. H. Du, Y. Pu, R. Adur, P. C. Hammel, and F. Y. Yang, Phys. Rev. B **88**, 100406 (2013).

[28] Y. Sun, Y. Y. Song, H. Chang, M. Kabatek, M. Jantz, W. Schneider, M. Wu, H. Schultheiss, and A. Hoffmann, Appl. Phys. Lett. **101**, 152405 (2012).

[29] T. Liu, H. Chang, V. Vlaminck, Y. Sun, M. Kabatek, A. Hoffmann, L. Deng, and M. Wu, J. Appl. Phys. **115**, 17A501 (2014).

[30] S. Mizukami, Y. Ando, and T. Miyazaki, Jpn. J. Appl. Phys. **40**, 580 (2001).

[31] M. J. Hurben and C. E. Patton, J. Appl. Phys. **83**, 4344 (1998).

[32] C. E. Patton, Phys. Rev. **179**, 352 (1969).

[33] T. Inui and N. Ogasawara, IEEE Trans. Magn. **13**, 1729 (1977).

[34] M. Sparks, *Ferromagnetic-Relaxation Theory* (McGraw-Hill, New York, 1964).

[35] K. Ando, S. Takahashi, J. Ieda, Y. Kajiwara, H. Nakayama, T. Yoshino, K. Harii, Y. Fujikawa, M. Matsuo, and S. Maekawa, J. Appl. Phys. **109**, 103913 (2011).

[36] E. Popova, N. Keller, F. Gendron, L. Thomas, M. C. Brianso, M. Guyot, M. Tessier, and S. S. P. Parkin, J. Vac. Sci. Technol. A **19**, 2567 (2001).

[37] M. Kubota, K. Shibuya, Y. Tokunaga, F. Kagawa, A. Tsukazaki, Y. Tokura, and M. Kawasaki, J. Magn. Magn. Mater. **339**, 63 (2013).

[38] A. Patterson, Phys. Rev. **56**, 978 (1939).

[39] T. Kikkawa, K.-i. Uchida, S. Daimon, Z. Qiu, Y. Shiomi, and E. Saitoh, Phys. Rev. B **92**, 064413 (2015).

[40] M. Agrawal, V. I. Vasyuchka, A. A. Serga, A. Kirihara, P. Pirro, T. Langner, M. B. Jungfleisch, A. V. Chumak, E. Th. Papaioannou, and B. Hillebrands, Phys. Rev. B **89**, 224414 (2014).

[41] A. Kehlberger, U. Ritzmann, D. Hinzke, E.-J. Guo, J. Cramer, G. Jakob, M. C. Onbasli, D. H. Kim, C. A. Ross, M. B. Jungfleisch, B. Hillebrands, U. Nowak, and M. Kläui, Phys. Rev. Lett. **115**, 096602 (2015).

[42] H. Adachi, J.-I. Ohe, S. Takahashi, and S. Maekawa, Phys. Rev. B **83**, 094410 (2011).

[43] S. M. Rezende, R. L. Rodríguez-Suárez, R. O. Cunha, J. C. L. Ortiz, and A. Azevedo, J. Magn. Magn. Mater. **400**, 171 (2016).

[44] J. C. Slonczewski, Phys. Rev. B **82**, 054403 (2010).

[45] M. Weiler, M. Althammer, M. Schreier, J. Lotze, M. Pernpeintner, S. Meyer, H. Huebl, R. Gross, A. Kamra, J. Xiao, Y.-T. Chen, H. J. Jiao, G. E. W. Bauer, and S. T. B. Goennenwein, Phys. Rev. Lett. **111**, 176601 (2013).